João Miguel Sanches
Andrew F. Laine · Jasjit S. Suri *Editors*

Ultrasound Imaging

Advances and Applications

Springer

Ultrasound Imaging

João Miguel Sanches • Andrew F. Laine
Jasjit S. Suri
Editors

Ultrasound Imaging

Advances and Applications

Springer

Editors
João Miguel Sanches
Department of Bioengineering
Institute for Systems and Robotics
Instituto Superior Técnico
Technical University of Lisbon
Lisboa
Portugal
jmrs@ist.utl.pt

Jasjit S. Suri
Biomedical Technologies, Inc.
Denver, CO, USA
and
Idaho State University (Affiliated)
Pocatello, ID, USA
jsuri@comcast.net

Andrew F. Laine
Department of Biomedical Engineering
Columbia University
New York
USA

ISBN 978-1-4614-1179-6 e-ISBN 978-1-4614-1180-2
DOI 10.1007/978-1-4614-1180-2
Springer New York Dordrecht Heidelberg London

Library of Congress Control Number: 2011939302

Preface

Diagnostic and therapeutic Ultrasound has recently taken an explosive growth for better safer, economic, mobile and high quality healthcare. This technology is very appealing for medical applications because it is non-ionizing, non-invasive and is available in most of the medical and clinical facilities. Its low cost, when compared with other medical image modalities, makes it one of the preferred tools for medical monitoring, follow-up and diagnosis. Besides the traditional fields of cardiology and obstetrics, where it is extensively used for long time, it has become also very useful in the diagnosis of diseases of the prostate, liver and coronaries and carotids atherosclerosis.

However, Ultrasound images present poor quality, very low signal to noise ratio and a lot of artifacts. The extraction of useful information from Ultrasound data for diagnosis is a challenge task that makes this medical image modality a very active field of research. The difficulties are being overcome and novel and advanced methods are being proposed for detection, characterization and segmentation of abnormalities in several organs. In fact, Ultrasound application range is vast, covering almost all organs, including the brain where *Transcranial Doppler* (TCD) Ultrasound is very important to assess the brain vasculature.

This book presents some of the recent advances in Ultrasound imaging technology covering several organs and techniques in a *Biomedical Engineering* (BME) perspective. The focus of the book is in the algorithms, methodologies and systems developed by multidisciplinary research teams of engineers and physicians for *Computer-Aided Diagnosis* (CAD) purposes.

Cardiovascular and cancer, the most common life-threatening diseases in western countries, are two of the most important topics focused in the book. However, other advanced issues are also presented such as *Intravascular Ultrasound* (IVUS), 3D and 4D Ultrasound and Ultrasound in *Computer-Aided Surgery* (CAS). Some chapters are direct contributions from medical research groups where Ultrasound has also received great attention in the last decade. By this, new techniques based on Ultrasound were introduced in the clinical practice for diagnosis and therapeutics, mainly in hospital facilities.

Main Feature of the Book

The book contains 14 chapters distributed by 3 sections. It covers a wide range of topics from the physics and statistics associated with the Ultrasound data, in a signal processing point of view, up to high level application tools for CAD based on Ultrasound.

Section 1: Image Formation and Preprocessing

In this section the image formation process is addressed and new statistical models describing the ultrasonic signal are proposed. Reduction of Ultrasound noise, called de-speckling, and textural characterization of tissues are considered.

Section 2: Ultrasound Atherosclerotic Plaque Imaging

Here, the important problem of atherosclerotic plaque characterization is addressed. Methods to assess the severity of the disease are described, such as measuring the *Intima/ Media Thickness* (IMT), as well as new scores to quantify the risk of vascular accident.

Section 3: Advanced Applications

This section covers a wide range of applications involving morphological and textural segmentation of structures from ultrasound images. Detection and characterization of focal lesions in the thyroid, breast and prostate and textural characterization of diffuse diseases of the liver are the main topics.

Contents

Contributors

Al-Nashash, Hasan American University of Sharjah, UAE, hnashash@aus.edu

Angelini, Elsa Associate Professor of Computer Science: Image & Signal Processing, Telecom ParisTech, 46 rue Barrault, 75013 Paris, France, elsa.angelini@telecom-paristech.fr

Balocco, Simone Computer Vision Center, Campus UAB, Edifici O, Bellaterra, Spain

University of Barcelona, Gran Via de Les Cortes Catalanes, 585, 08007 Barcelona, Spain, balocco.simone@gmail.com

Carlier, Stephane G. UZ Brussel, Department of Cardiology, Brussels, Belgium, sgcarlier@hotmail.com

Ciompi, Francesco Computer Vision Center, Campus UAB, Edifici O, Bellaterra, Spain

University of Barcelona, Gran Via de Les Cortes Catalanes, 585, 08007 Barcelona, Spain, fciompi@maia.ub.es

Duan, Qi National Institute of Neurological Disorders and Stroke, National Institutes of Health, 10 Center Drive, Building 10, Room B1D728, MSC 1065, Bethesda, MD 20892-1065, USA, Qi.Duan@nih.gov

Fernandes e Fernandes, José Instituto Cardiovascular de Lisboa and Faculty of Medicine, University of Lisbon, Portugal, jff@me.com

Fernandes e Fernandes, Ruy Instituto Cardiovascular de Lisboa and Faculty of Medicine, University of Lisbon, Portugal, ruyfernandes@mac.com

Ferré, Josepa Mauri Hospital universitari Germans Trias i Pujol, Carretera de Canyet s/n. 08916 Badalona, Spain, jmauri.germanstrias@gencat.cat

Gatta, Carlo Computer Vision Center, Campus UAB, Edifici O, Bellaterra, Spain

University of Barcelona, Gran Via de Les Cortes Catalanes, 585, 08007 Barcelona, Spain, cgatta@cvc.uab.es

Gonçalves, Isabel Department of Clinical Sciences, Experimental Cardiovascular Research Unit, Lund University, Malmo University Hospital, Malmo, Sweden, mgoncalvesadv@mail.telepac.pt

Katouzian, Amin Heffner Biomedical Imaging Lab, Biomedical Engineering Department, Columbia University, 1210 Amsterdam Ave., 373 Eng. Terrace, New York, NY 10027, amin.katouzian@cs.tum.edu

Konofagou, Elisa Associate Professor of Biomedical Engineering and Radiology, 351 Engineering Terrace, 1210 Amsterdam Avenue, 8904 New York, NY 10027, ek2191@columbia.edu

Laine, Andrew F. Vice-Chair, Professor of Biomedical Engineering and Radiology (Physics), 351 Engineering Terrace MC-8904, Biomedical Engineering Department, 1210 Amsterdam Avenue, Columbia University, MC-8904 New York, NY 10027, laine@columbia.edu

Loizou, Christos P. Department of Computer Science, School of Sciences, Intercollege, 92 Ayias Phylaxeos Str., P.O. Box 51604, CY-3507, Limassol, Cyprus, loizou.christos@ucy.ac.cy

Marinho, Rui Tato Liver Unit, Department of Gastroenterology and Hepatology, Hospital de Santa Maria, Medical School of Lisbon, Lisbon, Portugal, rui.marinho@mail.telepac.pt

Meiburger, Kristen M. Biolab, Department of Electronics, Politecnico di Torino, Corso Duca degli Abruzzi, 24, 10129 Torino, Italy, kristen.meiburger@polito.it

Molinari, Filippo Biolab, Department of Electronics, Politecnico di Torino, Corso Duca degli Abruzzi, 24, 10129 Torino, Italy, filippo.molinari@polito.it

Nicolaides, Andrew Vascular Screening and Diagnostic Centre, London, UK

Department of Biological Sciences, University of Cyprus, Nicosia, Cyprus, anicolaides1@gmail.com

Pantziaris, Marios Cyprus Institute of Neurology and Genetics, Nicosia, Cyprus, pantzari@cing.ac.cy

Pareek, Gyan Division of Urology, Section of Minimally Invasive Urologic Surgery, The Warren Alpert Medical School of Brown University, Rhode Island Hospital, 2 Dudley Street, Suite 174, Providence, RI 02905, USA, gyan_pareek@brown.edu

Patel, Sutchin R. Division of Urology, Section of Minimally Invasive Urologic Surgery, The Warren Alpert Medical School of Brown University, Rhode Island Hospital, 2 Dudley Street, Suite 174, Providence, RI 02905, USA, sutchin_patel@yahoo.com

Pattichis, Constantinos S. Department of Computer Science, University of Cyprus, Nicosia, Cyprus, pattichi@ucy.ac.cy

Pedro, Luís Mendes Instituto Cardiovascular de Lisboa and Faculty of Medicine, University of Lisbon, Portugal, lmendespedro@clix.pt

Pujol, Oriol Computer Vision Center, Campus UAB, Edifici O, Bellaterra, Spain

University of Barcelona, Gran Via de Les Cortes Catalanes, 585, 08007 Barcelona, Spain, oriol@maia.ub.es

Qaddoumi, Nasser N. American University of Sharjah, UAE, nqaddoumi@aus.edu

Radeva, Petia Computer Vision Center, Campus UAB, Edifici O, Bellaterra, Spain

University of Barcelona, Gran Via de Les Cortes Catalanes, 585, 08007 Barcelona, Spain, petia@cvc.uab.es

Ribeiro, Ricardo Institute for Systems and Robotics and Instituto Superior Tócnico/Technical University of Lisbon, Lisbon, Portugal

Escola Superior de Tecnologia da Saúde de Lisboa, Lisbon, Portugal, ricardo.ribeiro@estesl.ipl.pt

Sanches, João Miguel Institute for Systems and Robotics, Department of Bioengineering from the Instituto Superior Técnico/Technical University of Lisbon, Portugal, jmrs@ist.utl.pt

Seabra, José Institute for Systems and Robotics, Department of Bioengineering from the Instituto Superior Técnico/Technical University of Lisbon, Portugal, mail2jseabra@gmail.com

Sturm, Bernhard Manager, Signal and Image Processing, Volcano Corporation, 2870 Kilgore Road, Rancho Cordova, bsturm@volcanocorp.com

Suri, Jasjit S. Biomedical Technologies, Inc., Denver, CO, USA

Idaho State University (Affiliated), Pocatello, ID, USA, jsuri@comcast.net

Zeng, Guang MBF Bioscience Inc. Williston, VT, USA, gzeng@clemson.edu

Part I
Image Formation and Preprocessing

RF Ultrasound Estimation from B-Mode Images

José Seabra and João Miguel Sanches

Abstract This chapter describes a method to estimate/recover the ultrasound RF envelope signal from the observed B-mode images by taking into account the main operations usually performed by the ultrasound scanner in the acquisition process.

The proposed method assumes a Rayleigh distribution for the RF signal and a nonlinear logarithmic law, depending on unknown parameters, to model the compression procedure performed by the scanner used to improve the visualization of the data.

The goal of the proposed method is to estimate the parameters of the compression law, depending on the specific brightness and contrast adjustments performed by the operator during the acquisition process, in order to revert the process.

The method provides an accurate observation model which allows to design robust and effective despeckling/reconstruction methods for morphological and textural analysis of Ultrasound data to be used in *Computer Aided Dagnosis* (CAD) applications.

Numerous simulations with synthetic and real data, acquired under different conditions and from different tissues, show the robustness of the method and the validity of the adopted observation model to describe the acquisition process implemented in the conventional ultrasound scanners.

1 Introduction

Ultrasound statistical-based image processing for denoising, segmentation, and tissue characterization is an attractive field of research nowadays [1–3] and may positively influence some diagnostic decisions in the near future.

J. Seabra (✉) • J.M. Sanches
Institute for Systems and Robotics, Department of Bioengineering from the Instituto Superior Técnico/Technical University of Lisbon, Portugal
e-mail: mail2jseabra@gmail.com; jmrs@ist.utl.pt

J.M. Sanches et al. (eds.), *Ultrasound Imaging: Advances and Applications*,
DOI 10.1007/978-1-4614-1180-2_1, © Springer Science+Business Media, LLC 2012

It is widely recognized that speckle in B-mode Ultrasound (BUS) images arises from the coherent interaction of random scatterers within a resolution cell when a certain anatomical region is scanned. The common model for speckle formation assumes a large number of scatterers where the sum of signals may be formulated according to a typical phasors random walk process [4]. This condition, known as fully developed speckle, determines Rayleigh statistics for the *Envelope Radio-Frequency* (ERF) data [5]. In addition, different nonlinear processing operators are used to improve the visualization of the displayed image, here termed B-mode image. In particular, the amplitude of the ERF signal is logarithmically compressed and nonlinearly processed so that a larger dynamic range of weak to strong echoes can be represented in the same image.

The compressed data, typically acquired in a polar grid, is in turn interpolated and down-sampled in order to convert it to a Cartesian grid that is more appropriated for visualization in the rectangular monitors of the scanners. Finally, in a clinical setting, physicians typically adjust other parameters such as brightness and contrast to improve image visualization.

Many research work has been developed for speckle reduction aiming at providing clearer images for visualization [6]. However, very few approaches either focusing on speckle reduction or tissue classification take into account the pre-processing operations used to create the BUS images [7, 8]. Studies based on image processing from BUS images naturally need to follow a rigorous acquisition protocol, otherwise results will be non-reproducible and non-comparable since they will depend on the kind of ultrasound equipment and on each specific operating conditions. To avoid these difficulties some researchers [9–11] use the RF signal extracted directly from the ultrasound machine. However, this kind of data is not usually available at the scanners and is only provided for research purposes. In fact, besides the previously referred transformations of re-sampling, coordinate transformation, and logarithmic compression (cf. Fig. 1), the B-mode observed images are the result of other proprietary nonlinear mappings specific of each scanner that is usually not known and not documented .

In this chapter we show that, despite the lack of knowledge about the complete processing operations performed in the scanner, it is possible to revert the compression operation and compensate for the contrast and brightness adjustments performed by the operator during the exam. The interpolation is also addressed. The estimated *Log-Compression Law* (LCL) is able to provide an image more compatible with the physics of the image formation process than the B-mode one that may be used to design more accurate and effective denoised algorithms.

The remainder of this chapter is organized as follows. In Sect. 2 it is made a review of the most relevant work published about ultrasound image decompression and estimation of operating settings over the last years. Section 3 formulates the *Log-Compression* model and describes the statistics associated with the compressed image. In addition, simulations of the most significant operations affecting the statistical properties of the original data are shown and some observations are drawn about the way the shape of the distributions are affected. Subsequently, Sect. 4 details the method to estimate the parameters of the compression law,

specifically the contrast ($\hat{a}$) and brightness ($\hat{b}$) parameters. Section 5 first tests the effectiveness of estimating the decompression parameters with the proposed method using synthetic ultrasound data. To further investigate how realistic the proposed model is, the decompression method is applied to a real BUS image, from which the raw data is known, and comparison between original and estimated data is made.

The robustness of the decompression method is also evaluated using real images acquired under different operating conditions and a detailed interpretation of the obtained results is performed. Finally, *Goodness of Fit* (GoF) [12] tests are conducted in estimated ERF images to sustain the hypothesis that most envelope RF data can be well modeled by Rayleigh statistics. Section 6 concludes the study about decompression and envelope RF estimation from BUS data.

2 Related Work

A considerable amount of work dedicated to speckle suppression and tissue characterization relies on accurate statistical models for RF data. Such models albeit being ideally and robustly tailored to describe the envelope data in different conditions throughout the image, are not feasible and practical because RF data is usually not available. Thus, there is a need to develop realistic observation models that incorporate the most significant nonlinear processing operations affecting the envelope data, when only BUS images are provided. In order to compute the RF intensity signal it becomes crucial to (1) explain the statistics of the compressed signal and (2) invert the logarithmic compression and other nonlinear signal processing performed by the ultrasound machine. Commercial ultrasound scanners perform a set of operations on the RF signal, e.g., log-compression and interpolation [13], that change the statistical distribution of the complex raw RF signal which is no longer *Circular Symmetric Complex Gaussian* (CSCG) [14] and, therefore, the Rayleigh statistics of the ERF signal are no longer valid.

Seminal work conducted in [7, 15, 16] have addressed the analytic study of log compressed Rayleigh signals in medical ultrasound images. From thereon, several decompression strategies were developed aiming at estimating some of the nonlinear processing parameters [17–19] or providing an estimate of the envelope RF data [8, 20, 21]. In order to compute the ERF intensity signal, the logarithmic compression and other nonlinear operations must be inverted. A common model for the compression law used in the literature is the following

$$I_{\text{BUS}} = a \log(I_{\text{ERF}}) + b, \tag{1}$$

where a and b are unknown parameters. The work developed in [20] demonstrated that such mapping is able to approximately invert the compression algorithms employed by a number of different ultrasound machine manufacturers, given that the parameters are originally known. The additive parameter, b, does not affect the shape

of the statistics used to speckle because it only shifts the distribution function which does not happen with the gain parameter a. The study developed by Crawford et al. [20] proposed a systematic method to compensate for nonlinear amplification based on several measurements based on a calibrated phantom, while the study reported by Kaplan et al. [15] requires accessing the data before processing which is not feasible in most commercial machines.

The work from Prager et al. [8] introduced the fractional moments iterative algorithm for recovering the envelope intensity signal from B-Mode data using speckle patches. In such patches, where fully developed speckle holds, the envelope intensity signal, $\mathbf{Y}_p$, can be estimated by inverting the compression mapping,

$$\mathbf{Y}_p = \exp\left(\frac{\mathbf{Z}_p}{a}\right), \tag{2}$$

where $\mathbf{Z}_p$ is the B-Mode intensity on a given patch, p. According to [5], $\mathbf{Y}_p$ follows approximately an exponential distribution,

$$p(\mathbf{Y}_p) = \frac{1}{2\sigma^2}\exp\left(\frac{-\mathbf{Y}_p}{2\sigma^2}\right), \tag{3}$$

where the nth order moment is given by [22],

$$\langle \mathbf{Y}_p^n \rangle = (2\sigma^2)^n \Gamma(n+1) = \langle \mathbf{Y}_p \rangle^n \Gamma(n+1), \tag{4}$$

where $\Gamma(n)$ is the Gamma function. Therefore, the normalized moments are,

$$\frac{\langle \mathbf{Y}_p^n \rangle}{\langle \mathbf{Y}_p \rangle^n} = \Gamma(n+1). \tag{5}$$

This approach [8] compares the measured normalized moments on known speckle patches, $\mathbf{Y}_p$, with the theoretical expected values for an exponential distribution. The optimal value of the contrast parameter, a, can then be found by minimizing the difference between these two set of values. This algorithm produces similar results to the faster approach proposed in [15] for pure logarithmic compression, but also works in the presence of nonlinear mapping where the Kaplan [15] formula does not apply.

A more recent work presented by Marques et al. [21] and used in a 3D US reconstruction problem enables to model the nonlinear compression considering that the ERF data is Rayleigh distributed. The estimation of the log compression parameters is simultaneously performed with the image reconstruction procedure by optimizing the same objective function (PDF of the unknown parameters). Such parameters are obtained by considering the theoretical expressions for the mean and standard deviation of the Fisher–Tippet distribution [22] early demonstrated to be a feasible model for the compressed data [7].

Although the estimator of b has shown to be biased, this work presented promising results particularly in terms of image reconstruction. It has been shown that the reconstruction algorithm performs better when compensation is considered. The estimated images and profiles obtained by compensating the log compressed images are sharper, presenting a larger dynamic range, and the anatomical details are more clearly visible when compared with those obtained assuming no compression.

3 Log-Compression Model

Figure 1 depicts the processing block diagram of a generic ultrasound imaging system, including the most significant operations performed on the RF signal generated by the ultrasound probe: (1) interpolation and grid geometry conversion, from polar to rectangular to appropriate image display, (2) logarithmic compression, used to reduce the dynamic range of the input echo signal to match the smaller dynamic range of the display device and to accentuate objects with weak backscatter [13], (3) contrast, a, and (4) brightness, b adjustments. Some equipments perform an automatic adjustment of the parameters a and b which can further be tuned by the operator to improve image visualization in each specific exam. The model displayed in Fig. 1, illustrating the *Log-Compressed Law*, allows to simulate the generic processing operations of the ultrasound equipment, and to recover, whenever the original raw data is not available, an estimate of the ERF image.

As shown in Sect. 5 the interpolated data is better described by a Gamma distribution than by a Rayleigh one. However, the results displayed also show only a marginal improvement of the Gamma distribution with respect to the Rayleigh model, mainly at the transitions. Therefore, here, the interpolation is not taken into account in the designing of the ERF estimation algorithm.

The *Log-Compression model* (LCM) described in this section assumes a fully developed speckle noise formation model to describe the ERF image formation process. This condition is valid when images are reasonably homogeneous and

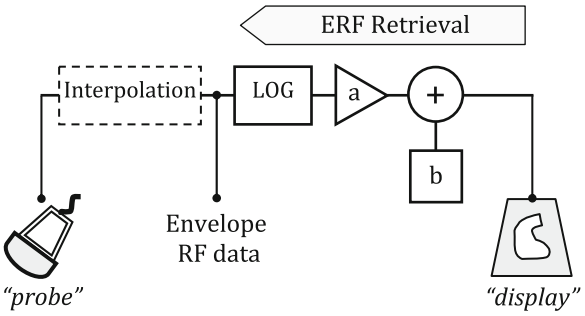

Fig. 1 Block diagram of the generic processing operations of an ultrasound imaging system

do not show high intensity scattering sites. Under these assumptions the ERF signal intensity can be described by a Rayleigh distribution [23], whose parameters, $\Sigma = \{\sigma_{i,j}\}$, associated with each pixel intensity of the ERF image, $y_{i,j}$, are related to the tissue acoustic properties [24] at the corresponding location, $x_{i,j}$.

Let $\mathbf{Z} = \{z_{i,j}\}$ be a $N \times M$ BUS image corrupted by speckle where each pixel is generated according to the following LCL,

$$z_{i,j} = a \log(y_{i,j} + 1) + b, \tag{6}$$

where (a, b) are unknown parameters used to model the contrast and brightness of the observed image, respectively. In the assumption of fully developed speckle the pixels of the ERF image, $Y = \{y_{i,j}\}$, are Rayleigh distributed [25]

$$p(y_{i,j}) = \frac{y_{i,j}}{\sigma_{i,j}^2} \exp\left(-\frac{y_{i,j}^2}{2\sigma_{i,j}^2}\right), \tag{7}$$

where $\sigma_{i,j}$ is the parameter of the distribution to be estimated. Consequently, the distribution of the observed pixels, $z_{i,j}$, given by $p(z) = \left|\frac{\mathrm{dy}}{\mathrm{dz}}\right| p(y)$ [14] corresponds to

$$p(z_{i,j}) = \frac{y_{i,j}(y_{i,j} + 1)}{a\sigma_{i,j}^2} \exp\left(-\frac{y_{i,j}^2}{2\sigma_{i,j}^2}\right). \tag{8}$$

Figure 2a–d simulates the BUS image formation process. The pixel intensities of the noisy image, displayed in Fig. 2b, were generated from Rayleigh distributions with parameters corresponding to the pixel intensities of the phantom displayed in Fig. 2a. To illustrate how the most relevant operations performed by the ultrasound scanner affect the statistical properties of the ERF signal the following simulations are performed. The noisy image is first interpolated and then compressed according to (6) and the final result, displayed in Fig. 2d, represents a typical image obtained with ultrasound equipment.

Figure 2e, f presents the shape of the data distribution throughout the processing operations for different contrast and brightness parameters used in (6). In general, the transformed image is significantly different from the original data from both statistical (histogram) and visual appearance points of view.

Only in the case of the interpolation operation the differences are not very relevant. The histogram of the independent Rayleigh distributed pixels inside the window k_y (see Fig. 2b) is not significantly different from the histogram of pixels inside the window k_y^i (see Fig. 2b). See both histograms displayed in Fig. 2e.

The effect of the interpolation operation is mainly low pass filtering the data leading to a slight reduction on the intensity variance of the transformed image. Variations on the brightness parameter, b, shift the distribution of the transform data along the gray-scale axis, as shown in (Fig. 2e). Moreover, as expected, the dynamic range parameter, a, produces the effect of compressing or stretching the distribution as a decreases or increases, respectively (Fig. 2f).

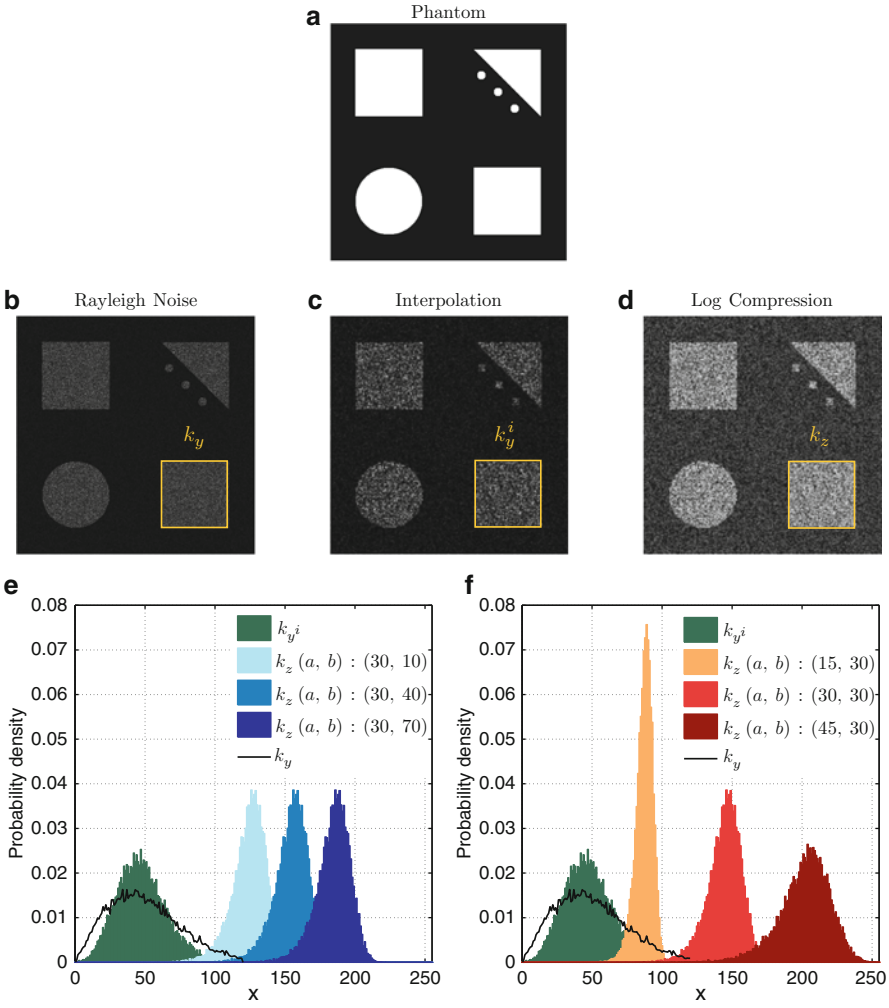

Fig. 2 BUS image formation model, starting from a phantom object (**a**). The method for generating synthetic BUS images includes corruption with Rayleigh noise (**b**), interpolation (**c**), and application of the LCL (**d**). Probability densities in k_y and k_y^i, and k_z when the parameters a (**e**) and b (**f**) are made variable

In the next section the estimation procedure to estimate the parameters a and b form (6) is described in order to decompress the data and estimate the unobserved ERF image, $y_{i,j}$, from the observed ultrasound B-mode one, $z_{i,j}$, by using the transformation

$$y_{i,j} = \exp\left(\frac{z_{i,j} - \hat{b}}{\hat{a}}\right) - 1, \tag{9}$$

where $(\hat{a}, \hat{b})$ are the estimated contrast and brightness parameters.

4 Estimation of Decompression Parameters

This method described here to estimate the *Log-Compression* parameters in (6) is an improved version of the method described in [21].

The estimation of the compression parameters (a,b) would be easier if the Rayleigh parameter, $\sigma_{i,j}$, was known. However, it is not known and varies across the image.

Let us approximate (9) by $y \approx \exp\left(\frac{z-b}{a}\right)$, the distribution (8) can be written as follows

$$p(z) = \frac{2}{a}\exp\left(-\theta - \exp(-\theta)\right), \tag{10}$$

where $\theta = \log(2\sigma^2) - 2\dfrac{z-b}{a}$. Equation (10) defines the *Fisher-Tippet* distribution [22], also known as double exponential. The mean and standard deviation (SD) of this distribution are:

$$\mu_z = \frac{a}{2}\left[\log(2\sigma^2) - \gamma\right] + b, \tag{11}$$

$$\sigma_z = \frac{\pi a}{\sqrt{24}}, \tag{12}$$

where $\gamma = 0.5772...$ is the Euler–Mascheroni constant.

To overcome the difficulty associated with the lack of knowledge of $\sigma_{i,j}$ let us now consider small $n \times m$ windows, $w_{i,j}$, centered at each pixel (i,j). The distribution parameters $\sigma_{k,l}$ within these small windows are assumed constant and equal to the parameter of the corresponding center pixel, $\sigma_{i,j}$, to be estimated.

If $a_{i,j}$ is assumed constant inside the small window $w_{i,j}$ it can be easily derived from (12)

$$\hat{a}_{i,j} = \sqrt{24}\frac{\sigma_{z_{i,j}}}{\pi}, \tag{13}$$

where $\sigma_{z_{i,j}}$ is the standard deviation of the observations inside the small window $w_{i,j}$

The parameter a, which is considered constant across the image, is estimated by averaging the parameters $\hat{a}_{i,j}$:

$$\hat{a} = \frac{1}{NM}\sum_{i,j=1}^{N,M}\hat{a}_{i,j}. \tag{14}$$

The estimation process of b is more challenging than the estimation of a, thus requiring a more elaborated and complex procedure. Let us consider the set of $n \times m = L$ unknown non compressed pixels $\mathbf{y} = \{y_{k,l}\}$ inside the window $w_{i,j}$ as being independent and identically Rayleigh distributed with parameter $\sigma_{i,j}$

$$p(y_{k,l}|\sigma_{i,j}) = \frac{y_{k,l}}{\sigma_{i,j}^2}\exp\left(-\frac{y_{k,l}^2}{2\sigma_{i,j}^2}\right). \tag{15}$$

As shown in [21], the distribution of the minimum of $\mathbf{y}$, $t = \min(\mathbf{y})$, is also Rayleigh distributed with parameter $\sigma_{i,j}^2/L$

$$p(t|\sigma) = \frac{t}{\sigma_{i,j}^2/L} \exp\left(-\frac{t^2}{2\sigma_{i,j}^2/L}\right). \tag{16}$$

The minimum of the observed pixels inside the window $w_{i,j}$, $\mathbf{z} = \{z_{k,l}\}$ where $z_{k,l} = a\log(y_{k,l}+1)+b$, is

$$\begin{aligned} s = \min(\mathbf{z}) &= a\log(\min(\mathbf{y})+1)+b \\ &= a\log(t+1)+b, \end{aligned} \tag{17}$$

which means

$$b = s - a\log(t+1). \tag{18}$$

The distribution of b, computed by $p(b|s,\sigma_{i,j}) = |\mathrm{d}t/\mathrm{d}b|p(t|\sigma_{i,j})$, is therefore given by

$$p(b|s,\sigma_{i,j}) = \frac{L}{a\sigma_{i,j}^2} t(t+1)\exp\left(-\frac{L}{2\sigma_{i,j}^2}t^2\right), \tag{19}$$

where $t = \exp\left(\frac{s-b}{a}\right) - 1$. $\sigma_{i,j}$, the distribution parameter associated with the (i,j) pixel, is not known neither constant across the image. However, if it is considered constant inside the small window $w_{i,j}$ a local estimation of b is possible to derive. Since $\mathbf{y}$ is assumed Rayleigh distributed an appropriated approximation for $\sigma_{i,j}$ is

$$\tilde{\sigma}_{i,j} = \sqrt{\frac{1}{2nm}\sum_{k,l}\tilde{y}_{k,l}^2}, \tag{20}$$

where

$$\tilde{y}_{k,l} = \exp\left(\frac{z_{k,l}-\tilde{b}}{a}\right) - 1, \tag{21}$$

and

$$\tilde{b} = \min(\mathbf{z}). \tag{22}$$

Since b is not known $\tilde{b} \approx b$ is used in (21) instead of b. As it will be shown in the section of experimental results this approximation is valid.

Let $\hat{b}_{i,j}$ be the estimated value of b, computed from the pixels within the small window $w_{i,j}$. Its value is nothing more than the expected value of b with respect to the distribution (19) with the parameter computed in (20),

$$\hat{b}_{i,j} = \int_{-\infty}^{\infty} b_{i,j} p(b_{i,j}|s, \tilde{\sigma}_{i,j}) \mathrm{d}b_{i,j}. \tag{23}$$

The closed form solution of (23) is difficult to compute and a numeric approach is adopted, such that:

$$\hat{b}_{i,j} = \sum_{k=1}^{L} b_{i,j}(k) p(b_{i,j}(k)|s, \tilde{\sigma}_{i,j}), \tag{24}$$

where $b_{i,j}(k) = ks/(L-1), k = 0, 1, ..., L-1$ are L uniformly distributed values in the interval $[0, s]$, since it is assumed that $b \geq 0$ and from (18), $b \leq s$.

The global value of b, once again, is obtained by averaging the estimated $\hat{b}_{i,j}$:

$$\hat{b} = \frac{1}{NM} \sum_{i,j=1}^{N,M} \hat{b}_{i,j}. \tag{25}$$

The estimated parameters $(\hat{a}, \hat{b})$ are then used to revert the Log-compression performed by the ultrasound equipment in order to recover the original RF signal:

$$y_{i,j} = \exp\left(\frac{z_{i,j} - \hat{b}}{\hat{a}}\right) - 1, \tag{26}$$

which is assumed, in the remainder of this chapter, to be Rayleigh distributed.

5 Experimental Results

In this section, different results are presented aiming to assess the performance of the proposed method. First, the accuracy on the decompression parameters (a, b) estimation procedure is computed by using synthetic ultrasound data. The validity of the decompression method is also assessed by using real data. A comparison is made between the original ERF image, obtained from raw data, and the estimated ERF image, obtained from the BUS image.

In addition, the adequacy and robustness of the ERF image retrieval method is investigated in the real case using two sets of experiments, including the application of the decompression method in (1) different BUS images acquired with fixed brightness and contrast parameters and (2) static BUS images acquired with variable operating parameters.

Finally, GoF tests with Rayleigh and Gamma distributions are conducted in estimated ERF images which enables to support the hypothesis that most envelope RF data can be well modeled by these two distributions. The interpretation of the obtained results suggest the use of the simpler Rayleigh distribution to decompress that data.

The decompression method is initially tested in synthetic data by using Monte Carlo tests. Particularly, in this experiment it is intended to assess the estimation accuracy of the decompression parameters, (a,b), for different images and amounts of noise. For each pair of decompression parameters 50 Monte Carlo runs were performed. In each run, two different types of synthetic images are used to revert the compression method and estimate the parameters $(\hat{a},\hat{b})$, uniform and non uniform. Three uniform synthetic images are corrupted with Rayleigh noise with parameters $\sigma^2 = \{10^2, 10^3, 5 \cdot 10^3\}$. The non uniform image is the Shepp–Logan phantom also corrupted by the same three different amounts of noise used with the uniform phantoms. In both cases the noisy images are interpolated and log-compressed according to (6).

Figure 3 presents the average and SD of the 50 estimated decompression parameters, $(\hat{a},\hat{b})$, obtained for each true pair (a,b), by using the first phantom (Fig. 3a) and the non-uniform Shepp–Logan phantom (Fig. 3b).

Similar results are obtained in both cases which suggests that the decompression method has similar behavior for uniform and non-uniform images, and its performance is apparently independent on the severity of speckle noise contamination. The later conclusion is confirmed in Fig. 3a where the observed results do not depend on the value of the Rayleigh parameter σ used to generate the noisy image.

In general, the estimation $\hat{a}$ is non biased and its SD increase mainly with a_0 (see Fig. 3a, b, top left). The variability of $\hat{a}$ tends to be less significant as b increases (see Fig. 3a, b, bottom left). The average values of the uncertainties associated with $\hat{a}$, $SD(\hat{a})/a_0$, are: 0.54%, 0.60%, and 0.60% for the uniform image with $\sigma^2 = 100, 1{,}000$, and 5,000, respectively, and 0.61% for the non-uniform image. As far as the ratio $SD(\hat{a})/a$ is concerned, the uncertainty associated with $\hat{a}$ is almost residual.

The estimation of b, $\hat{b}$, is also non biased (see Fig. 3a, b, top right). In particular, the average values of the uncertainties associated with $\hat{b}$, $SD(\hat{b})/b$, are: 2.4%, 2.4%, and 2.4% for the uniform image with $\sigma^2 = 100, 1{,}000$, and 5,000, respectively, and 2.3% for the non-uniform image. The uncertainty associated with the decompression parameter $\hat{b}$ increases linearly with a. In fact, this behavior is similar to the one obtained for $\hat{a}$, except for very small values of a, where the uncertainty about $\hat{b}$ increases with b (see Fig. 3a, b, bottom right).

The method here proposed is able to invert the compression operations when synthetic images are given. Moreover, it is important to study the feasibility of the method when raw data is provided by the manufacturer. Notice that the challenge of decompression from BUS images is only raised because raw data is generally not available in a clinical setting, thus limiting the application of algorithms which are based on statistical modeling of speckle or RF data.

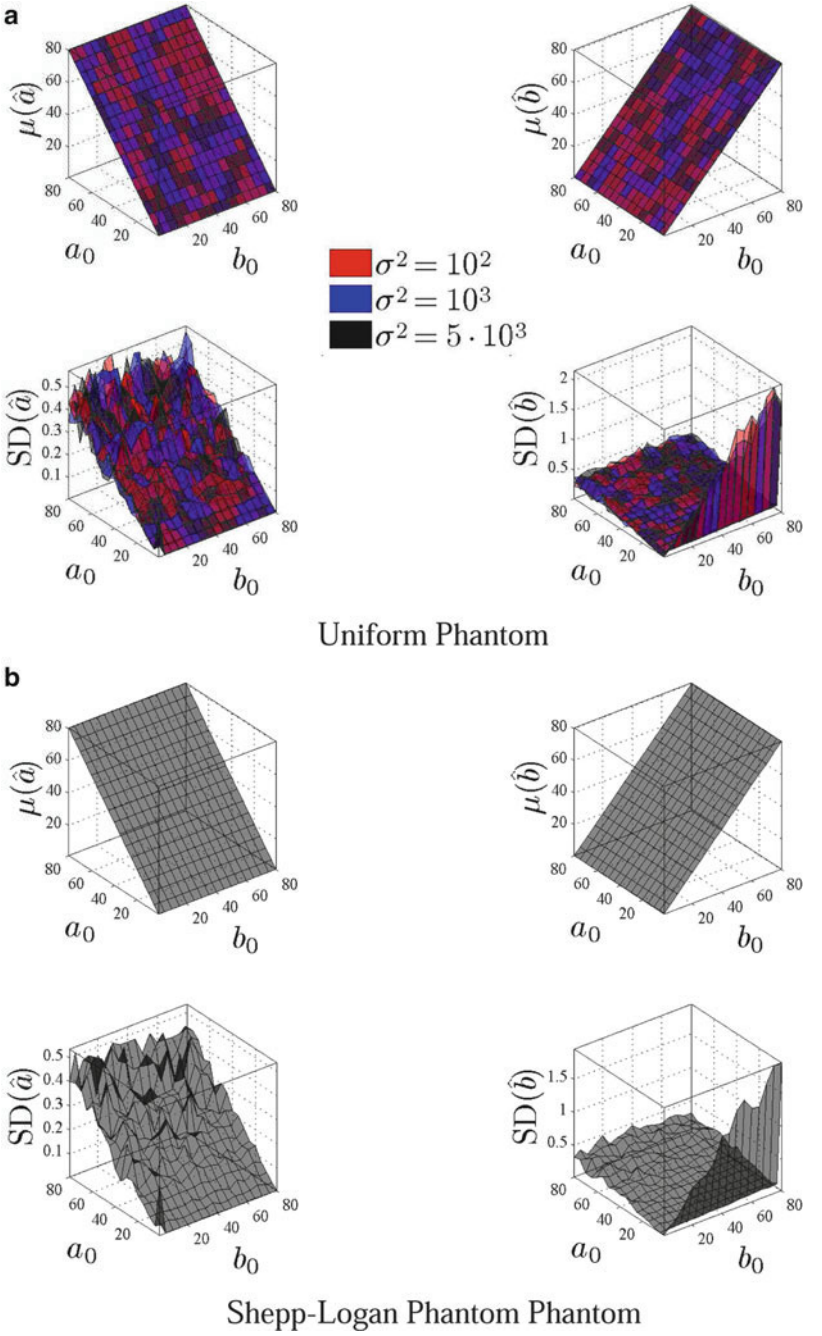

Fig. 3 Estimation of the decompression parameters using Monte Carlo tests. Performance is assessed by computing the mean and SD of ($\hat{a}$,$\hat{b}$) in simulated log compressed images of a noisy uniform image created with Rayleigh parameters (**a**) and noisy Shepp–Logan phantom (**b**)

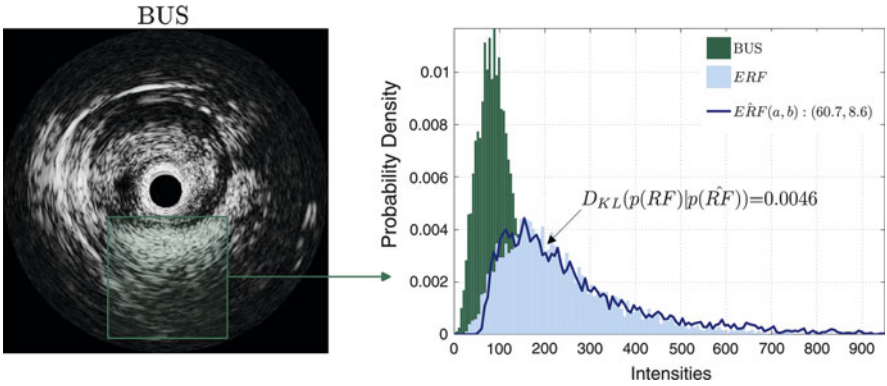

Fig. 4 Application of the RF image retrieval (decompression) method to a BUS image representing a coronary artery. PDFs of the BUS, original ERF, and estimated ERF images, extracted from a given ROI

Hence, in this study it was used an IVUS BUS image corresponding to a cut of the coronary artery (Fig. 4a) together with the RF image obtained from raw RF data, obtained with specialized equipment (Galaxy II IVUS Imaging System, Boston Scientific, Natick, MA, United States). The RF image retrieval(decompression) method is applied to the BUS image, resulting in an estimate of the envelope data, the $E\hat{R}F$ image. As shown in Fig. 4b, the statistical properties of the original and estimated ERF images are closely similar. This observation supports the adequacy of the proposed method to provide an estimate of the envelope RF data which resembles the original one.

So far the decompression method was validated using an IVUS image from which the raw data was known. Moreover, it is also pertinent to investigate the robustness of the method according to different acquisition settings and scenarios. To this purpose, the RF image retrieval method is tested under two different conditions: first, by changing the probe position and keeping the operating parameters constant, and second by maintaining the probe steady and varying the contrast and brightness parameters.

Figure 5a–c presents results of the application of the decompression method proposed in this chapter. In particular, three image sets were acquired for different anatomical structures/tissues by slightly changing the probe position between each image acquisition. For each set of RF estimated images, a homogeneous region was selected and its intensity histogram computed as shown in Fig. 6a–c (left). These results show that the statistical properties of the estimated RF images are comparable, suggesting that the decompression method is robust to small changes in image appearance. The decompression parameters from each image set are depicted in Fig. 6a–c (right). The SDs for $\hat{a}$ and $\hat{b}$ are $(3.83; 2.97)$, $(4.26; 2.01)$, and $(1.96; 1.80)$, respectively for each set of decompressed images, which shows that the uncertainty about the estimated LCL parameters is low in different imaging conditions.

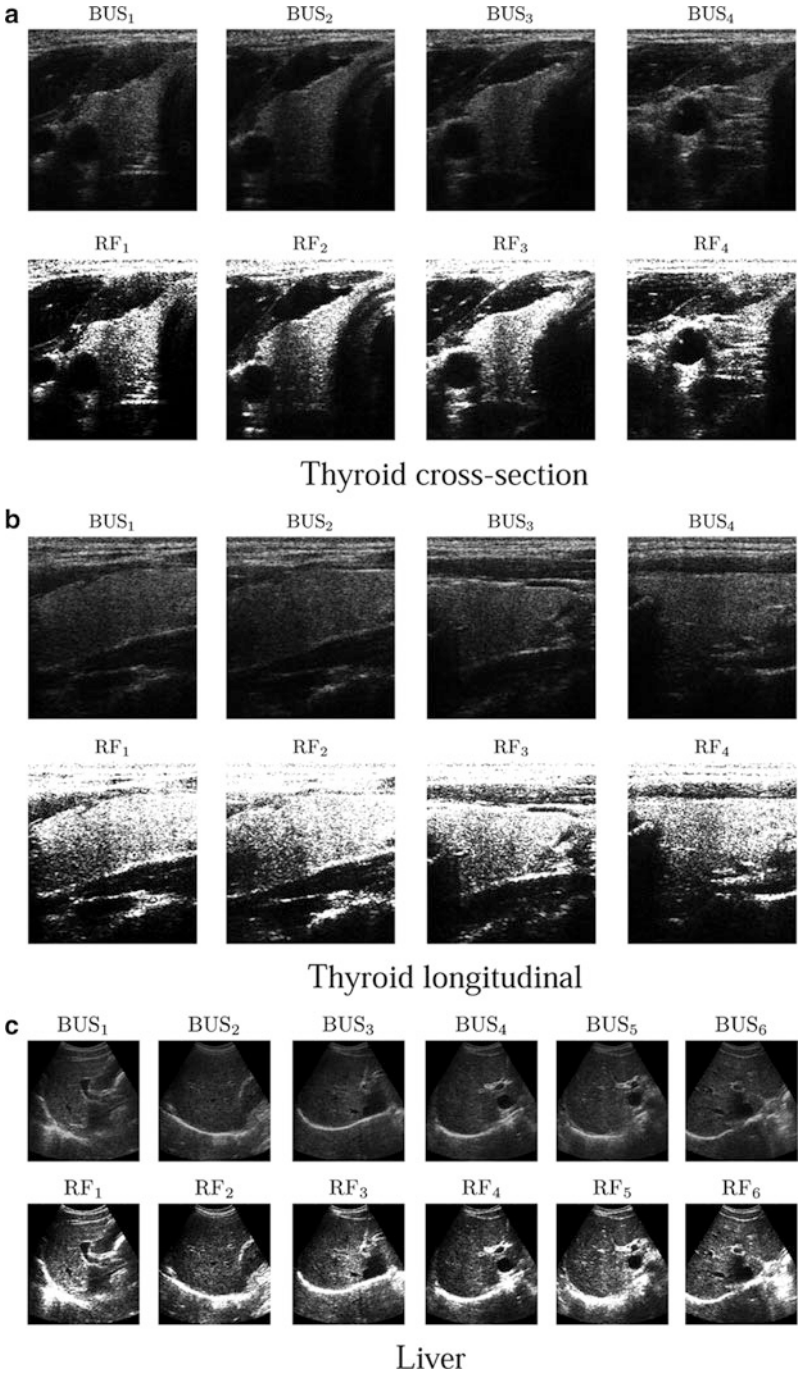

Fig. 5 Application of the decompression method to different sets of images acquired from different tissues using fixed operating conditions

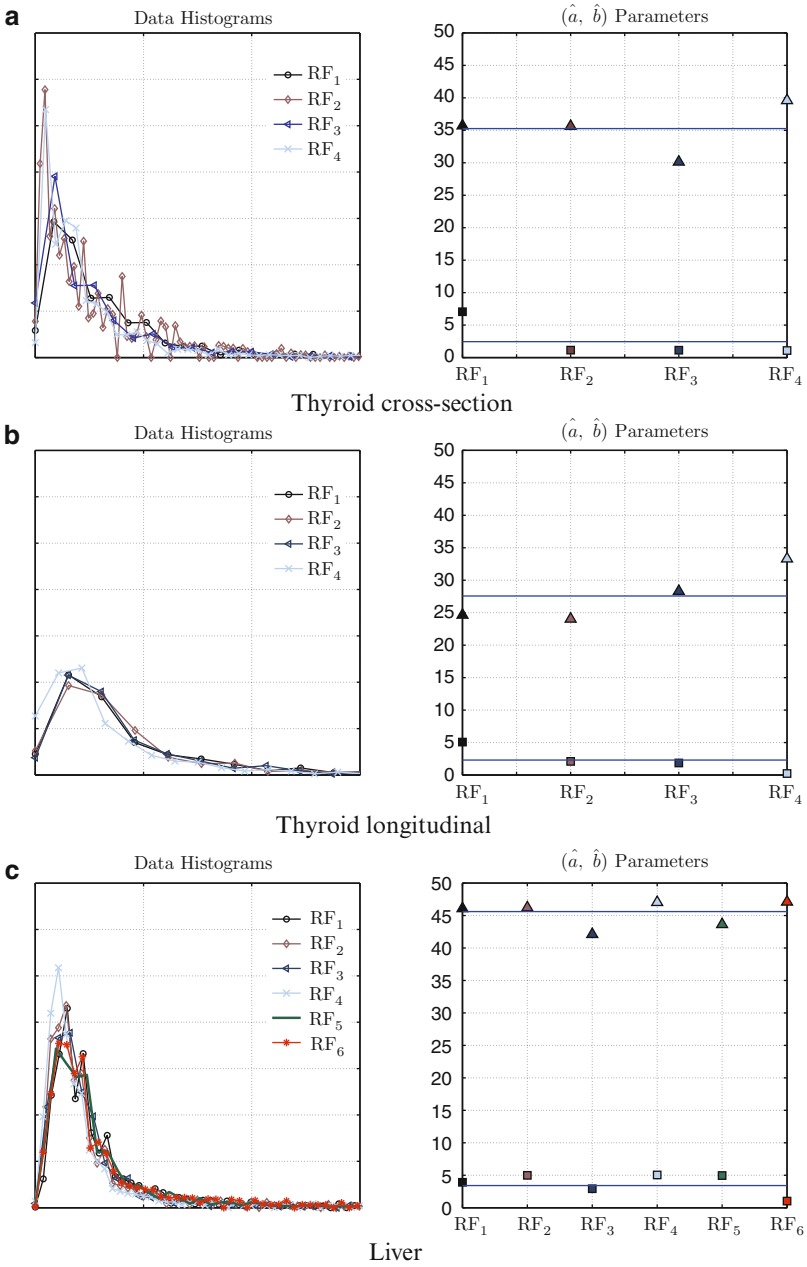

Fig. 6 (*Left side*) Data histograms extracted from regions of interest in the estimated ERF images, shown in Fig. 5. (*Right side*) Decompression parameters

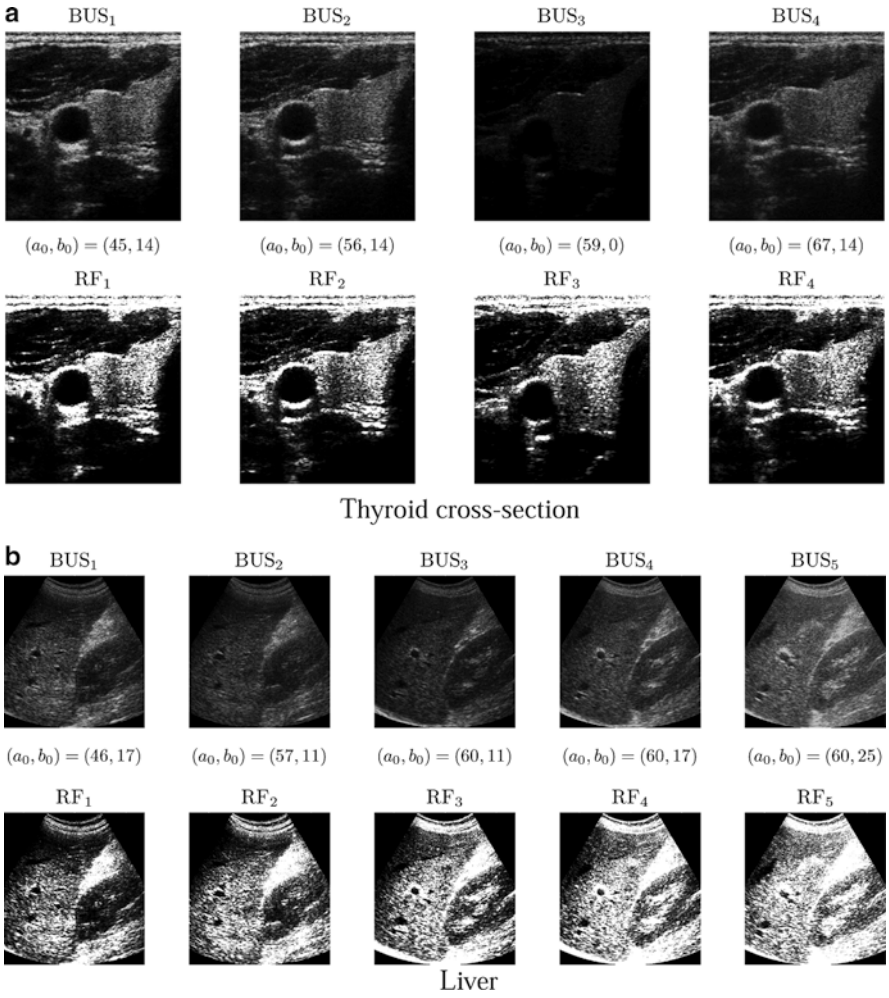

Fig. 7 Application of the decompression method to sets of images acquired from different tissues, acquired with a steady probe and variable operating parameters

As previously mentioned, the second experiment consisted in acquiring a series of BUS images by keeping the probe steady and varying the operating parameters. Results of the application of the decompression method in two different image sets are shown in Fig. 7. In terms of gray-scale image appearance, the obtained ERF images present similar dynamic range and brightness. Histogram analysis of data extracted from homogeneous regions in such images (Fig. 8a, b on the left) suggests similar statistical properties among the estimated ERF images. A comparison between the contrast and brightness parameters given by the US scanner with the estimated decompression parameters is given in Fig. 8a, b on the right. Although a

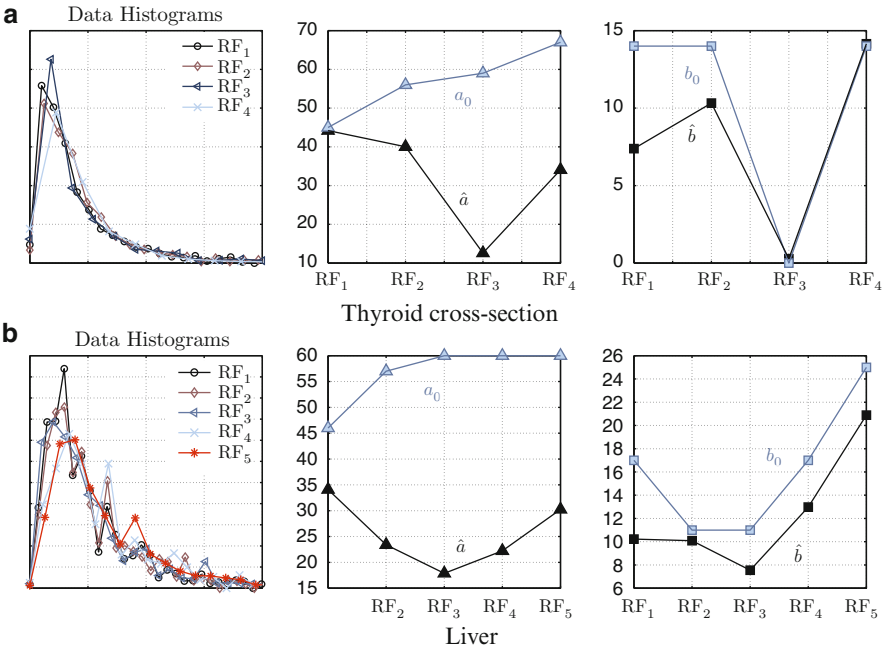

Fig. 8 (*Left side*) Data histograms extracted from regions of interest in the estimated ERF images, shown in Fig. 7. (*Right side*) Decompression parameters estimated with proposed method vs. machine operating settings

numerical comparison is naturally unfeasible because the equipment's settings may not directly correspond to the values assigned to the operating parameters being estimated, it is pertinent to investigate how the estimated parameters change with respect to the original settings of the machine. Considering the estimated parameters $\hat{a}$ these appear to change approximately in inverse proportion with respect to the original dynamic range settings a. Moreover, the estimated parameters $\hat{b}$ vary roughly in direct proportion according to the original linear gain settings b. These results support the ability of the proposed method to estimate the decompression parameters, evoking a similarity association between these values and the settings defined with the ultrasound equipment.

Results aiming at assessing the adequacy and robustness of the proposed decompression method in the aforementioned real cases are detailed in Table 1. Besides the decompression parameters obtained for each image of the data set, it is also shown the Kullback–Leibler distance [26] of each distribution with respect to the first distribution of each set. Observations taken from Table 1 support, from a quantitative point of view, the robustness of the decompression method in estimating precisely the decompression parameters and the ERF images.

It is relevant to investigate whether the assumptions made initially about the adequacy of the Rayleigh distribution to model the pixel intensities in ERF images

Table 1 Decompression parameters $(\hat{a}, \hat{b})$, and Kullback–Leibler distances computed from ERF data histograms, as result of the application of the RF image retrieval under two different conditions (constant and variable operating parameters)

		Thyroid cross-section			Thyroid longitudinal			Liver		
Parameters	ID	$\hat{a}$	$\hat{b}$	$d_{KL}(h_1, h_{ID})$	$\hat{a}$	$\hat{b}$	$d_{KL}(h_1, h_{ID})$	$\hat{a}$	$\hat{b}$	$d_{KL}(h_1, h_{ID})$
Constant	RF_1	35.71	7.05	–	24.65	5.07	–	46.09	3.91	–
	RF_2	35.64	1.14	−1.61	24.04	2.10	0.02	46.22	4.98	−0.01
	RF_3	30.14	1.13	0.26	28.30	1.85	0.01	42.12	2.92	2.62
	RF_4	39.60	1.08	−0.84	33.30	0.22	−0.28	47.04	5.04	0.42
	RF_5							43.64	4.95	1.72
	RF_6							47.10	1.02	0.25
Variable	RF_1	57.17	3.18	–				34.09	10.22	–
	RF_2	44.20	7.38	2.40				23.41	10.09	0.11
	RF_3	40.02	10.32	2.10				36.35	0.02	3.28
	RF_4	12.60	0.28	4.02				17.88	7.55	0.81
	RF_5	34.07	14.15	5.01				22.23	12.90	1.02
	RF_6							30.26	20.89	1.27

are realistic or not. It is known that the assumption of fully developed speckle determines Rayleigh statistics for the amplitude of the envelope RF data, although the Gamma distribution seems to provide a better approximation [27, 28], mainly when interpolation is involved, which is the case.

Hence, the purpose of the study presented in Fig. 10 is to investigate whether the Rayleigh and Gamma distributions are capable of locally describing the estimated ERF images (Fig. 9). Given this, the *Maximum Likelihood* (ML) estimates of the Rayleigh and Gamma distribution were computed locally for each image. This computation is done in 8×8 sliding blocks with 2×2 overlapping borders, throughout the images. For each block the probability density functions (PDFs) are computed according to the ML-based Rayleigh and Gamma estimates. Moreover, a correlation coefficient measure is computed to compare each distribution with the data histogram, given by:

$$\rho_{xy} = \frac{\delta_{xy}}{\sigma_x \sigma_y}, \tag{27}$$

where δ_{xy} is the covariance matrix of the mentioned PDFs and σ_x and σ_y are their standard deviations. When the correlation coefficient, ρ_{xy}, is 1 it means the distribution under investigation (either Rayleigh or Gamma) perfectly models the local data. Figure 10 consists of color-scaled GoF maps, including the local comparison of ERF data vs. ML estimated Rayleigh distribution (Fig. 10a), ERF data vs. ML estimated Gamma distribution (Fig. 10b) and finally, Rayleigh vs. Gamma distribution (Fig. 10c).

In both cases, the Gamma distribution is able to better describe the data when compared to the Rayleigh distribution. An interesting observation is that the